remote sensing

Article

InSAR-Derived Shallow Rupture of the July 2025 Comapa Earthquake Sequence, Southern Guatemala, Along a Previously Unidentified Normal Fault

Jiuyuan Yang [1], Shenchang Gu [1], Huaiyang Zhang [1], Kaifeng Ma [1,*], Zhenjie Yao [1], Xiaohua Hou [2] and Tanyu Wang [1]

[1] College of Surveying and Geo-Informatics, North China University of Water Resources and Electric Power, Zhengzhou 450046, China; yangjiuyuan@ncwu.edu.cn (J.Y.); 202205115@stu.ncwu.edu.cn (S.G.); z20251151150@stu.ncwu.edu.cn (H.Z.); z20241151129@stu.ncwu.edu.cn (Z.Y.); wangtanyu1018@163.com (T.W.)

[2] College of Hydraulic and Architectural Engineering, Tarim University, Aral 843300, China; 120020025@taru.edu.cn

* Correspondence: makaifeng@ncwu.edu.cn

Highlights

What are the main findings?

- A previously unidentified moderate-angle NE-dipping normal fault is activated during the 2025 Comapa earthquake.
- Coseismic slip is mainly distributed within shallow depth beneath the high-altitude summit, modifying the local topography.

What are the implications of the main findings?

- Multi-view InSAR observations can accurately detect blind normal faults with no surface expression, thereby improving our understanding of regional subsurface seismogenic structures and seismic hazards.
- Moderate normal--faulting earthquakes play a significant role in lowering the local high topography and limiting the continuous uplift of the mountain range over repeated seismic cycles, highlighting the importance of normal-faulting earthquakes for modifying the local topography of southern Guatemala.

Abstract

On 29 July 2025, a shallow earthquake sequence, including an M_W 5.6 foreshock and an M_W 5.7 mainshock, occurred ~6 km southeast of Comapa, Southern Guatemala. As representative moderate-to-large crustal earthquakes in the tectonically complex North America-Caribbean-Cocos triple-junction region, the Comapa earthquake sequence offers an excellent chance to shed light on the regional subsurface fault structure, rupture kinematics, topographic evolution and tectonic stress changes through modern high-precision satellite geodetic observations. To date, no relevant geodetic and geological studies of this earthquake sequence have been conducted, and its fault geometry and source model thus remain poorly understood. In this study, we used Sentinel-1 Interferometric Synthetic Aperture Radar (InSAR) datasets from three different viewing geometries to derive high-resolution coseismic line-of-sight (LOS) surface deformation related to this earthquake sequence and then inverted the data for its fault geometric parameters and source model. An integrated analysis of geodetic inversion results, fault distribution and kinematics illustrates that the earthquake sequence ruptured a previously unmapped moderate-angle NE-dipping normal fault. Most coseismic slip of up to 0.6 m is distrib-

Academic Editors: Guo Chen, Wei Tang, Ling Huang and Amir Allahvirdi-Zadeh

Received: 23 September 2026
Revised: 25 November 2026
Accepted: 26 November 2026
Published: 29 November 2026

Copyright: © 2026 by the authors. Licensee MDPI, Basel, Switzerland. This article is an open access article distributed under the terms and conditions of the Creative Commons Attribution (CC BY) license.

uted within the 0–6 km shallow depth beneath the high-altitude summit where the concentrated subsidence lowers the local high topography. Moreover, we investigate the stress interaction between the July 2025 Comapa earthquake and large historical M_W > 7.0 earthquakes around the subduction zone of southern Guatemala and find that these historical earthquakes produce ~0.03 MPa of stress change at the epicentral region of the 2025 earthquake, possibly advancing the occurrence of the Comapa earthquake. Our further Coulomb stress modeling reveals that the shallow part of the San Vicente fault and the eastern segment of the Jalpatagua fault have experienced coseismic stress loading with maximum magnitudes of 0.04 MPa and 0.17 MPa, respectively, indicating elevated rupture potential that demands sustained geodetic monitoring. Our study highlights the significance of normal-faulting earthquakes for shaping the local topography of Southern Guatemala.

Keywords: InSAR observations; Comapa earthquake; normal-faulting structure; stress interaction; topography effects

1. Introduction

Guatemala lies at the triple junction of the North American, Caribbean, and Cocos plates, representing one of the most tectonically complex and seismically active plate boundary regions in Central America (Figure 1a,b) [1,2]. Ongoing subduction (a convergence rate of ~69–72 mm/yr) of the Cocos Plate underneath the Caribbean Plate along the Middle America Trench (MAT) and left-lateral transform motion at a relative rate of ~20 mm/yr along the North America-Caribbean plate boundary generate complex crustal deformation and high seismic activity throughout the tectonic region (Figure 1a,b) [3–7]. A series of strong earthquakes such as the 1976 M_W 7.5 earthquake, 1982 M_W 7.3 earthquake, 1983 M_W 7.0 earthquake, 2001 M_W 7.7 earthquake and 2012 M_W 7.4 earthquake occurred in Guatemala over recent decades, especially along the subduction zone (Figure 1b). Such frequent occurrence of strong earthquakes across Guatemala reflects complex tectonic processes that govern regional crustal stress accumulation and fault activation. Southern Guatemala, a critical tectonic subsection within Guatemala, experiences intense tectonic deformation primarily controlled by major NW-striking strike-slip structures and N-S-trending extensional structures, notably the Jalpatagua fault (JF), Ahuachapan fault (ACF), Ashapuco fault (APF), Guatemala City graben (GG) and Ipala graben (IG) (Figure 1c) [2,5]. As a prominent dextral strike-slip structure, JF extends aligned with the Central American Volcanic Arc (CAVA) and accommodates up to 7.6 mm/yr of forearc translation (Figure 1c) [5]. Meanwhile, moderate-to-high-angle normal faults, which bound the adjacent grabens and basins within the shallow crust, also exhibit high tectonic activity, facilitate localized crustal extension and possess substantial seismogenic potential (Figure 1c) [8,9].

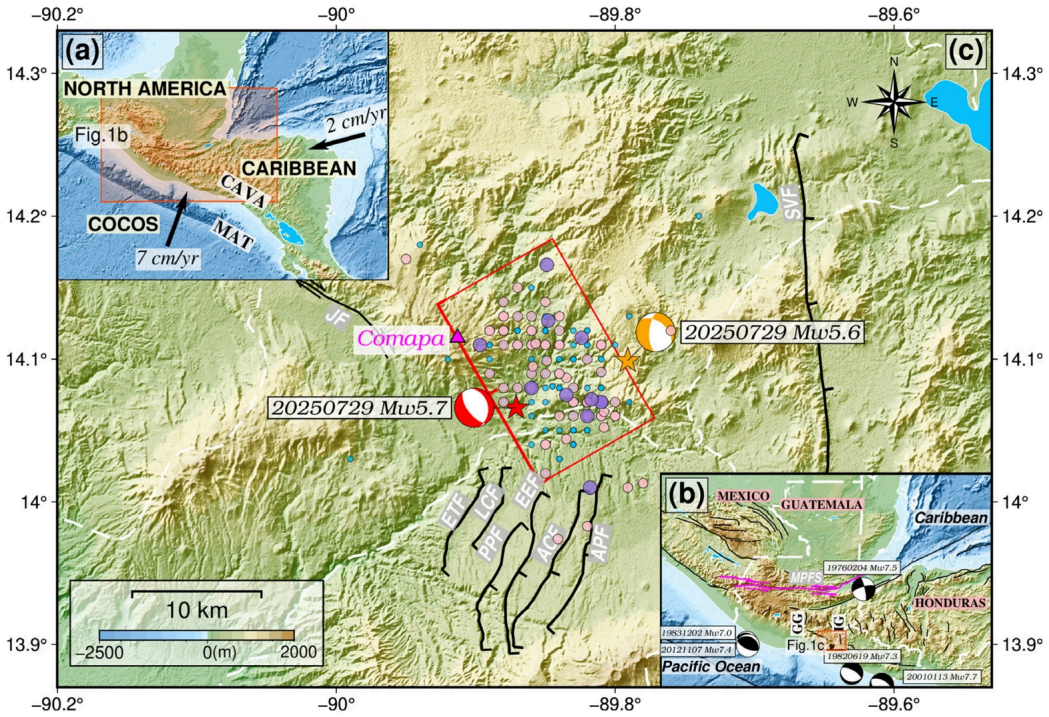


Figure 1. (**a**) Geological setting of western Central America and the Caribbean that illustrates the tectonic interactions among the North American, Caribbean, and Cocos tectonic plates. MAT: Middle America Trench; CAVA: Central American Volcanic Arc; (**b**) Tectonic setting of Guatemala. White dashed lines outline the national boundary regions of Guatemala. Faults are derived from the Caribbean and Central American active fault database [7]. MPFS: Motagua-Polochic fault system; GG: Guatemala City graben; IG: Ipala graben; (**c**) Tectonic map of the 29 July 2025 Comapa seismic sequence. Red and orange stars paired with beach balls mark the epicenters and focal mechanisms for the 29 July 2025 M_W 5.7 and M_W 5.6 Comapa earthquakes. The colorful circles represent $M_W \geq 2.0$ aftershocks reported by EMSC five months after the M_W 5.7 mainshock. Red thick line indicates the fault surface trace retrieved from the linear inversion. The topography on the hanging wall is higher than that on the footwall. ETF: El Tigre Fault; LCF: Las Chinamas Fault; PPF: Palo Pique Fault; EEF: El Espino Fault; ACF: Ahuachapan Fault; APF: Ashapuco Fault; SVF: San Vicente Fault; JF: Jalpatagua Fault.

On 29 July 2025 (21:21 UTC), a M_W 5.6 shallow normal foreshock struck approximately 6 km southeast of Comapa, Jutiapa Province, southern Guatemala, as reported by the United States Geological Survey (USGS; https://www.usgs.gov/). Only four minutes later (21:25 UTC), a second M_W 5.7 shallow normal mainshock occurred at 10 km depth (Figure 1c). The two earthquakes caused two fatalities, at least 26 injuries, damage to 1386 homes and widespread power outages across southern Guatemala (https://earthquake.usgs.gov/earthquakes/eventpage/us6000qw58/impact, accessed on 20 November 2026). Geologically, these two moderate-to-strong earthquakes are located southeast of the dextral strike-slip JF and north of the NE-striking active normal fault system (Figure 1c). Nevertheless, their epicenters correspond to high-relief terrain that lacks unambiguous surface fault geomorphology. This observation implies that the seismogenic structure is likely a blind fault, whose subsurface rupture geometry cannot be fully resolved solely from field-based geological surveys and thus requires geodetic constraint. In the five months following the July 2025 mainshock, the Euro-Mediterranean Seismological Centre (EMSC; https://www.emsc-csem.org/, accessed on 20 November 2026) recorded 229 aftershocks whose magnitudes fall between 2.0 to 5.0 (Figure 1c). The aftershocks define a single compact cluster with no spatial separation (Figure 1c), likely implying acti-

vation of the same structure during the earthquake sequence. These subsequent aftershocks further perturbed the previously weakened slopes and geologic structures, thus giving rise to delayed ground failures and progressive damage. Earthquake focal mechanisms provided by the Global Centroid Moment Tensor (GCMT; https://www.globalcmt.org/, accessed on 20 November 2026) and USGS imply that the 2025 M_W 5.7 Comapa earthquake ruptured along either a nearly NE-dipping moderate-angle normal fault or a SW-dipping steep normal fault (Table 1). The M_W 5.6 foreshock also nucleated on the similar rupture fault structure (Table 1). The occurrence of this earthquake sequence offers a valuable chance to understand the subsurface fault structure, rupture kinematics, topographic effects and tectonic stress in southern Guatemala by modern high-precision space geodetic observations, thus improving our knowledge of regional geodynamic processes and seismic hazard evaluation.

Table 1. Earthquake source properties of the 29 July 2025 M_W 5.7 Comapa earthquake.

Earthquake	Model	Lon, Lat (°)	Strike, Dip, Rake (°)	Length (km)	Width (km)	Depth (km)	Slip (m)	M_W
M_W 5.6 2025-07-29 21:21:47	USGS	−89.791, 14.099	307/183, 44/62, −138/−54	-	-	11.9	-	5.6
	GCMT	−89.84, 14.14	312/182, 44/58, −131/−58	-	-	13.6	-	5.6
M_W 5.7 2025-07-29 21:25:23	USGS	−89.871, 14.066	348/144, 31/62, −69/−102	-	-	10.0	-	5.7
	GCMT	−89.93, 14.15	330/162, 40/51, −99/−83	-	-	12.0	-	5.7
Uniform slip model		89.858, 14.094	330.3, 43.03, −72.09	7.0641	8.5391	0.9253	0.4203	-

Herein, we first apply Sentinel-1 ascending and descending InSAR datasets from three different viewing geometries to obtain the high-precision coseismic surface deformation of the 29 July 2025 Comapa earthquake sequence and further invert for fault geometrical parameters and spatially variable coseismic slip of the Comapa earthquakes. We also ascertain dip orientation of the seismogenic fault for this earthquake sequence by an integrated analysis of the detailed geodetic inversion and regional fault structure and kinematics and discuss the effect of this earthquake sequence on the regional topography effects. Then, we investigate stress interactions between the 2025 Comapa earthquake and historical M_W >7.0 earthquakes adjacent to the subduction zone of southern Guatemala. At last, we quantitatively compute the static Coulomb stress changes induced by the 2025 Comapa earthquake along the neighboring active faults so as to assess their possible implications for local seismic hazards.

2. InSAR Observations

Operated by the European Space Agency (ESA), the Sentinel-1 mission incorporates a system of C-band synthetic aperture radar (SAR) satellites dedicated to long-term Earth observation. Its Interferometric Wide Swath (IW) mode provides a swath width of ~250 km and serves as the main acquisition mode for ground-deformation monitoring [10]. Retrieving surface displacements from phase differences of two temporally separated SAR acquisitions, differential interferometric SAR (DInSAR) helps detect unmapped faults and constrain geometries of known seismogenic faults [11]. In this study, we adopt the two-pass DInSAR technology to generate coseismic interferograms for the

July 2025 M_W 5.7 Comapa earthquake based on the C-band Sentinel-1A satellite SAR images launched by ASF () [12,13]. Three coseismic interferograms spanning the July 2025 Comapa earthquake are formed from six Sentinel-1 Single Look Complex (SLC) data products captured in IW-TOPS mode (Table 2). During the SAR processing, co-registration is performed between primary (preseismic) and secondary (postseismic) SAR images to align their geometric configurations, which is essential for obtaining accurate interferometric phase differences. Afterwards, 30 m resolution SRTM DEM datasets from the open USGS EarthExplorer platform (https://earthexplorer.usgs.gov/) are adopted to eliminate flat-earth and terrain-related phase signals. To weaken phase noise interference and lift the signal-to-noise level of interferograms, the Goldstein filtering algorithm is applied to suppress noisy phase components, which also mitigates decoherence noise brought on by time and space baselines [14]. We mask out areas of coherence <0.4 and apply the minimum cost flow (MCF) method to perform the phase unwrapping processing [15]. Lastly, we geocode the coseismic interferograms to the WGS84 geographic coordinates. These processing steps help mitigate tropospheric phase artefacts induced by local micro-meteorological variations in the mountainous study region. Joint inversion of multi-view-geometry InSAR datasets further suppresses orbit-dependent atmospheric noise. Detailed InSAR processing procedures and uncertainty evaluations for atmospheric artefacts, orbital errors and coherence masking are provided in Supplementary Text S1. Coseismic ascending and descending interferograms (Figure 2a–c) present comparable deformation amplitudes and similar fringe patterns in agreement with the major motion away from the satellite, suggesting that surface deformation caused by 2025 Comapa earthquake sequence is dominated by subsidence. Much denser fringes at the western margin of the main deformation area relative to its eastern side across the ascending and descending interferograms (Figure 2a–c) implies that the east-dipping rupture fault may be the source fault of the Comapa events. As described above, we infer that the 2025 Comapa earthquake sequence likely ruptured an east-dipping normal fault, although further evidence is needed to confirm this inference. The maximum LOS displacement of the ascending interferogram amounts to ~20 cm, while the maximum LOS displacements of the two descending interferograms reach up to 18.5 cm and 15.8 cm, respectively (Figure 2d–f).

Table 2. Parameters of SAR datasets applied to derive coseismic deformation for the 29 July 2025 Comapa earthquake sequence.

Satellite	Track	Master Date	Revisit Date	Perb.B (m)	Inc.Angle	Azi.Angle
Sentinel-1	T26D	17 July 2025	10 August 2025	20.255	31.960	−77.956
Sentinel-1	T128D	24 July 2025	17 August 2025	−33.416	44.636	−78.4182
Sentinel-1	T136A	25 July 2025	6 August 2025	−69.024	44.366	79.804

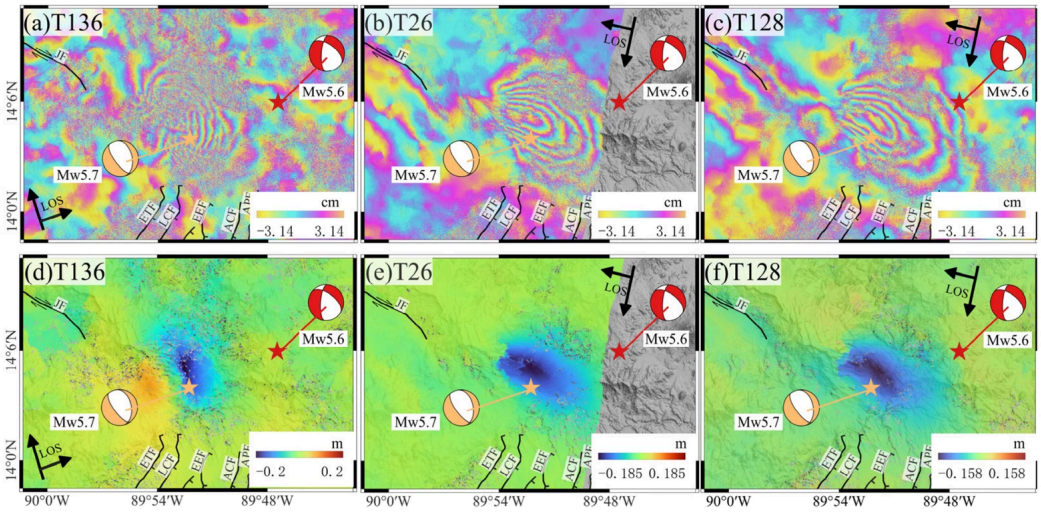


Figure 2. (**a**–**c**) are the observed ascending and descending coseismic interferograms of the 29 July 2025 Comapa earthquake sequence from Sentinel-1 satellite. (**d**–**f**) are corresponding coseismic deformation maps of the Comapa earthquakes from Sentinel-1 satellite (Table 2).

3. Geodetic Modeling

To discover the rupture behavior of the July 2025 Comapa earthquake sequence, we apply a resolution-adaptive spatial resampling algorithm to downsample the raw coseismic line-of-sight (LOS) displacement fields derived from Sentinel-1 interferometric stacks. Dense sampling was kept in the near-field deformation zone to preserve the coseismic signal, while far-field deformation regions were more sparsely sampled to reduce computational cost and avoid redundant observations. The derived coseismic LOS surface displacements are exploited to invert for seismogenic fault geometric parameters and coseismic slip of the Comapa earthquakes on the basis of the homogeneous isotropic elastic half-space rectangular dislocation theory [16]. In this study, given the relatively small magnitude and large hypocentral depth of the Mw 5.6 earthquake (Table 1), we infer that the most of the coseismic surface deformation is attributed to the Mw 5.7 earthquake and that little surface deformation is attributed to the Mw 5.6 earthquake. Then, a nonlinear inversion method is firstly adopted to determine fault geometric parameters under the assumption of a rectangular uniform-slip fault, and a linear inversion is further implemented to obtain the spatially variable slip distribution on the optimal fault plane.

3.1. Uniform Slip Model Inversion

Based on the foregoing descriptions of coseismic interferograms for the 2025 Comapa earthquake sequence and the published earthquake focal mechanisms from USGS and GCMT, we infer that a northeast-dipping normal fault is likely to account for the Comapa earthquake. During the nonlinear inversion, we assumed uniform slip on a single rectangular fault plane to solve for the globally optimal geometric parameters of the seismogenic fault for the 2025 Comapa earthquakes. The search intervals for strike, dip and rake are defined as [271°, 359°], [20°, 70°] and [−135°, 45°], respectively, while those for fault length and width are set as [0 km, 25 km] and [0 km, 25 km], respectively. A Marquardt nonlinear least-squares algorithm combined with grid search was adopted to achieve the minimum root-mean-square (RMS) misfit between InSAR-derived displacements and forward-modeled synthetic signals, avoiding local optimal solutions during parameter search [17]. To quantitatively evaluate the uncertainty of fault geometric parameters (fault location, length, width, depth, dip, strike, rake, uniform slip), we

implemented Monte Carlo synthetic tests with 100 independent groups of datasets contaminated with Gaussian noise. The optimal fault geometric parameters, along with their associated standard deviations, are acquired (Figure 3 and Table 1). Overall, the retrieved fault parameters are well-resolved with limited uncertainty ranges (Figure 3). As an example, the fault location uncertainties are less than 0.005° while the rake, dip and strike uncertainties remain less than 8.6° (Figure 3). The obtained uniform slip model indicates that the source fault extends 8.5 km along strike and 7.1 km down-dip with a strike of ~330° and a dip of ~43°. The rake of ~−72° suggests predominantly normal dip-slip accompanied by minor sinistral strike-slip component. The uniform slip reaches 0.42 m, and the top edge of the uniform fault plane is buried at a depth of ~0.9 km. Surface displacements predicted by the uniform-slip model show a good match with the observed coseismic deformation. However, relatively large residuals remain near the fault surface trace (Figure 4c,f,i). The RMS misfits between the observed and modeled surface deformation amount to 1.9 cm, 1.7 cm and 1.4 cm for the ascending and the two descending tracks, respectively.

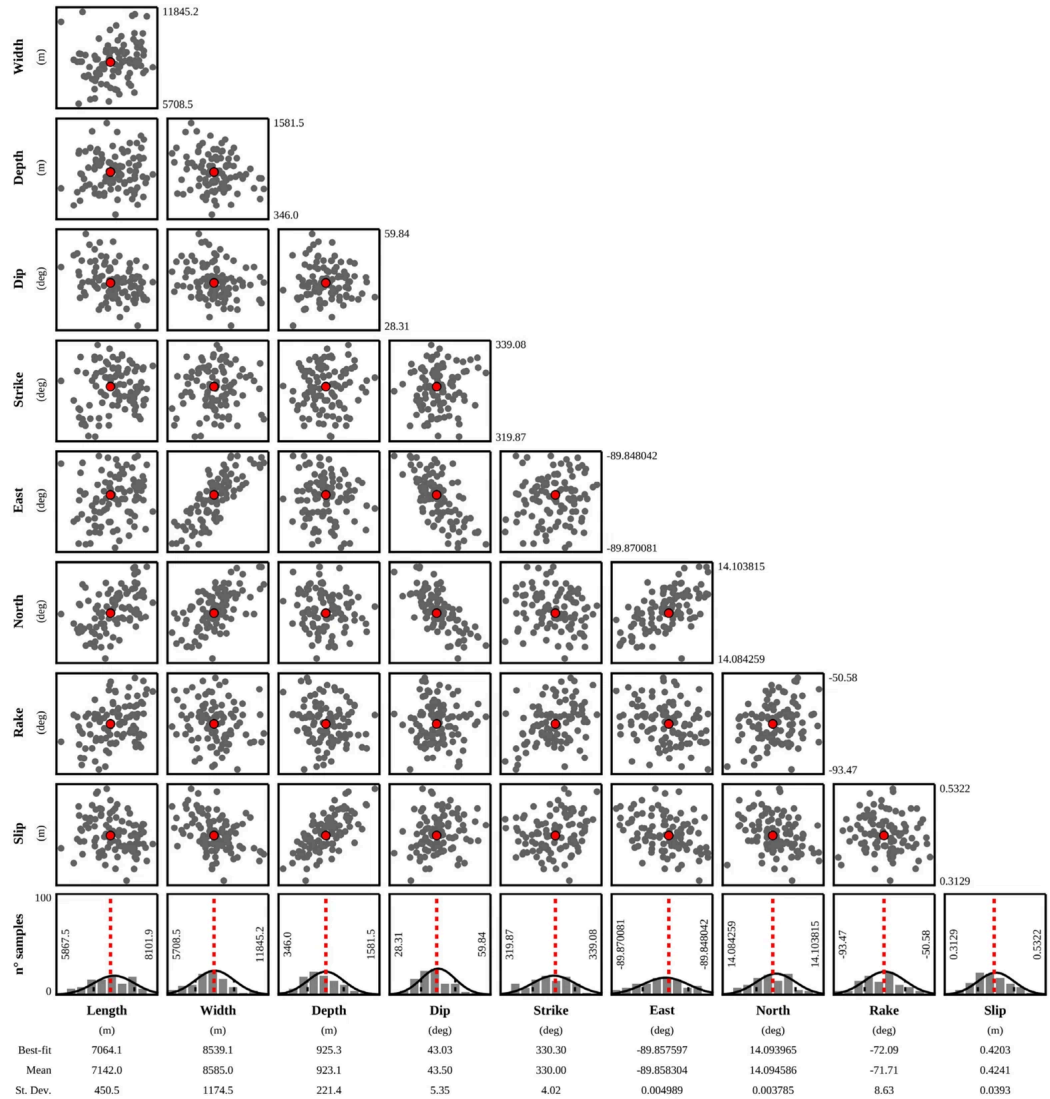


Figure 3. Probability density distributions of inverted fault geometric parameters for the north-east-dipping uniform-slip fault model of the 29 July 2025 Comapa earthquake sequence.

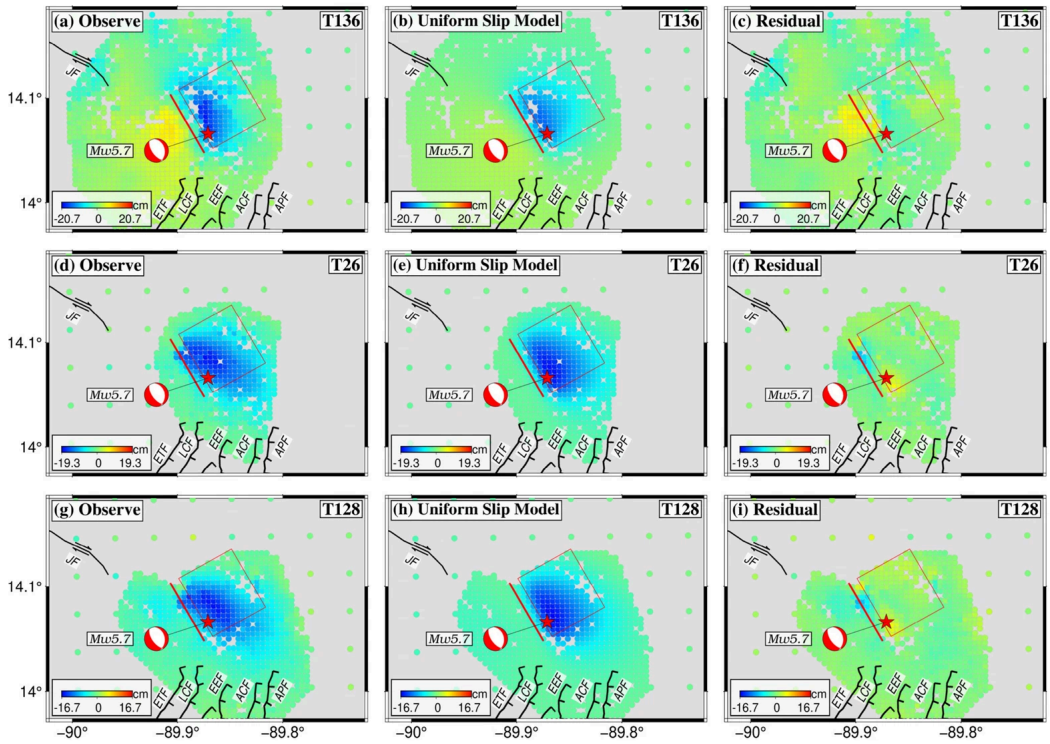


Figure 4. (**a**,**d**,**g**) are the observed coseismic surface deformation of the 29 July 2025 Comapa earthquake; (**b**,**e**,**h**) are the corresponding modeled deformation by the uniform slip model of the Comapa earthquake; (**c**,**f**,**i**) are residual maps. Red thick line and thin box exhibit the surface projection of the source fault and rupture plane, respectively, from the nonlinear inversion.

3.2. Coseismic Slip Distribution Inversion

With the fault location, dip and strike determined from the nonlinear inversion fixed, we extended the fault plane to 16 km × 14 km along strike and dip and discretized it into 1 km × 1 km regular sub-patches to invert for spatially variable slip distribution of the 2025 Comapa earthquake sequence. During the inversion, we constructed elastic Green's functions corresponding to each subfault unit and incorporated Laplace smoothing regularization into the least-squares objective function to suppress nonphysical oscillatory slip [18]. The inverted coseismic slip result (Figure 5) implies that the Comapa earthquake sequence is characterized by predominant normal faulting with minor sinistral strike-slip component and that the Comapa earthquake sequence accommodates the SW-NE-trending extensional strain through the hanging-wall subsidence of the source fault. Most coseismic slip is confined to depths ranging from 0 to 6 km, with the peak slip of ~0.6 m concentrated at 2.7 km depth (Figure 5). Notably, coseismic slip is mainly located beneath the high-altitude summit (Figures 1c and 5b). In high-altitude extensional settings, such normal-faulting earthquakes occurring repeatedly can subside hanging walls and lower the local high topography by reducing the gradient, thus limiting the continuous uplift of the mountain range and shaping the regional topography. Several slip patches of up to 0.3 m reach the surface (Figure 5b), implying a potential for surface rupture associated with this event. The RMS misfits between the observed and modeled deformation are 1.9 cm, 1.2 cm and 1.1 cm for the ascending and the two descending tracks. The coseismic slip distribution model yields a geodetic seismic moment of 1.08×10^{18} N·m that is equivalent to M_W 5.8. The geodetically derived seismic moment is larger than that reported by USGS and GCMT, which is likely caused by superposed deformation of the Mw 5.6 foreshock and Mw 5.7 mainshock within the observation period.

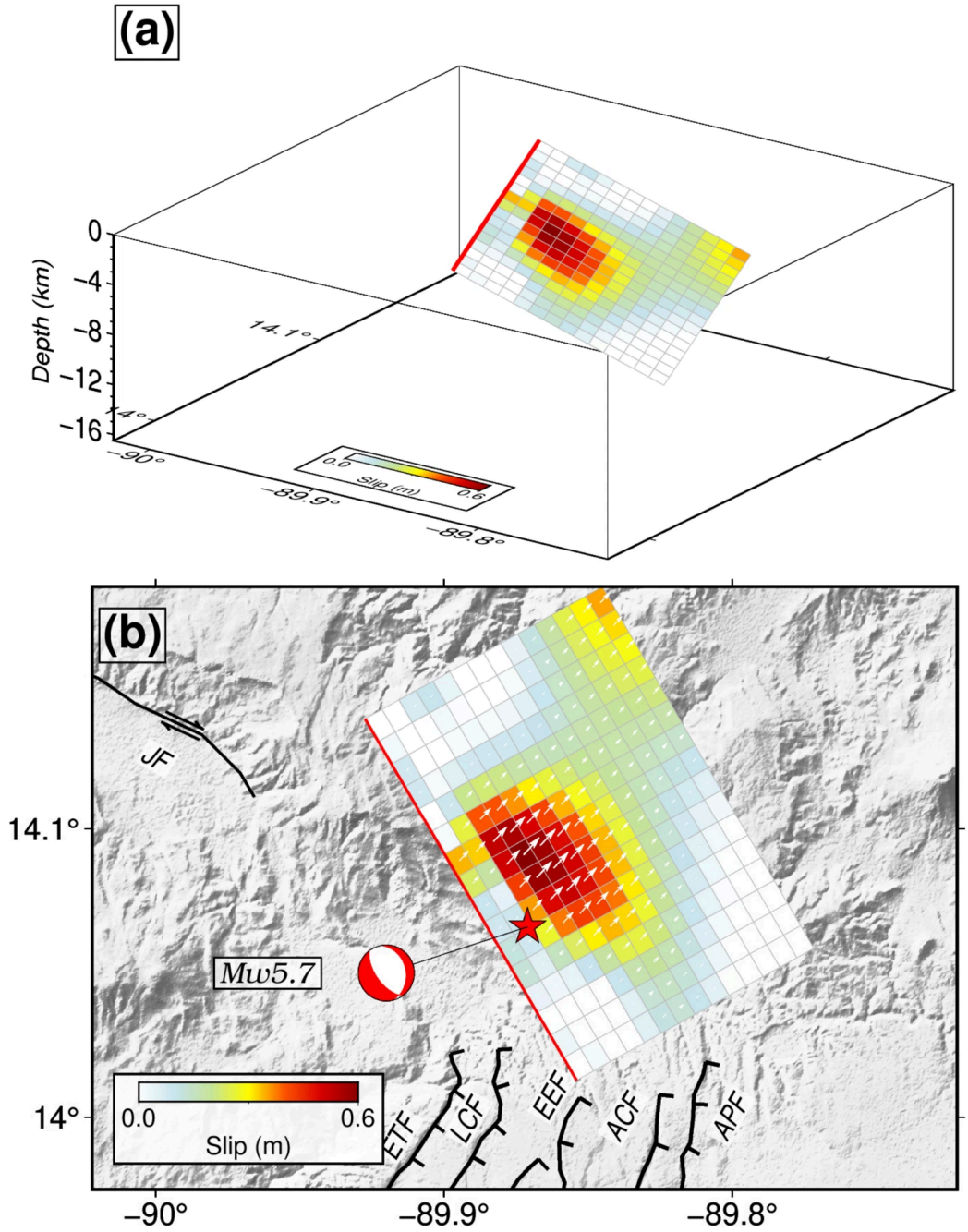


Figure 5. (**a**) is the three-dimensional (3D) perspective of the NE-dipping coseismic slip distribution model for the 29 July 2025 Mw 5.7 Comapa earthquake; (**b**) is the two-dimensional (2D) map view of the slip model. White arrows denote the direction of fault slip. Red thick line depicts the fault surface trace. The red star denotes the epicenter, and the beach ball represents the focal mechanism of this earthquake.

4. Discussion

4.1. Coseismic Rupture of 2025 Comapa Earthquake on a NE-Dipping or SW-Dipping Normal Fault?

Accurately identifying seismogenic fault plane for moderate normal earthquakes is vital to understanding earthquake nucleation, rupture behavior, landscape evolution and seismic hazard assessment. Earthquake focal mechanisms from GCMT and USGS (Table 1) indicate that the July 2025 M_W 5.7 Comapa earthquake is characterized by normal-faulting with possible rupture along either a SW-dipping or NE-dipping fault.

Given that no surface ruptures linked to the Comapa earthquake have been documented, it is not conclusive to ascertain the dipping direction of the seismogenic fault solely from the coseismic deformation fringe described in Section 2. For moderate normal-faulting events in this extensional orogenic setting, blind rupture often occurs beneath the surface without obvious geomorphic expression (Figure 1c), making it difficult to ascertain the location and dipping direction of the seismogenic fault from surface morphology. Moment tensor inversion from GCMT and USGS (Table 1) only provides two mathematically indistinguishable nodal planes and cannot intrinsically determine which one represents the real rupture plane, which demands independent geodetic constraints to distinguish the actual rupture plane from the auxiliary plane. Hence, to identify the optimal source fault plane, we seek to collect more supporting evidence, consisting of the detailed coseismic geodetic modeling, regional fault distribution and kinematics. Based on the fault plane solutions from GCMT and USGS (Table 1), we construct a new SW-dipping fault model to carry out the geodetic modeling. The search interval for strike is set as [91°, 179°], while all other parameters keep free. All inversion procedures are the same as those for the NE-dipping fault model described in Section 3. The SW-dipping coseismic slip model (a strike of ~123° and a dip of ~34°) reveals that the Comapa earthquake is characterized by normal dip-slip motion of up to ~0.9 m with a slight dextral strike-slip component (Figure 6). The overall coseismic deformation can be fitted, but the residuals between observed and modeled surface deformation within the major deformation area are much larger for the SW-dipping coseismic slip model (Figure 7) than those for the NE-dipping model (Figure 8). Thereinto, for the SW-dipping fault model, the RMS misfits between the observed and modeled deformation are 2.2 cm, 1.6 cm and 1.3 cm for the ascending and the two descending tracks. By contrast, the NE-dipping model achieves RMS misfits of 1.9 cm, 1.2 cm and 1.1 cm for the ascending and the two descending tracks, respectively. These pieces of evidence suggest that the NE-dipping fault plane is likely the seismogenic fault plane. In the vicinity of the Comapa earthquake, numerous nearly E-dipping normal faults such as APF, EEF, ETF and SVF are developed and accommodated the regional extensional deformation (Figure 1c). In general, the strike of such active faults shows good consistency with that of the NE-dipping rupture fault (Figure 1c) but is inconsistent with that of the SW-dipping rupture fault (Figure 6b). Furthermore, the mapped normal faults in the tectonically active Southern Guatemala typically develop with a moderate-to-high-angle dip [8,9]. However, the inverted dip (~34°) of the SW-dipping rupture fault is relatively lower, which conflicts with the regional fault structure. As a whole, according to the joint analysis of InSAR modeling results and regional tectonic structure, we interpret the NE -dipping normal fault as the actual rupture fault plane that generated the 2025 M_W 5.7 Comapa earthquake.

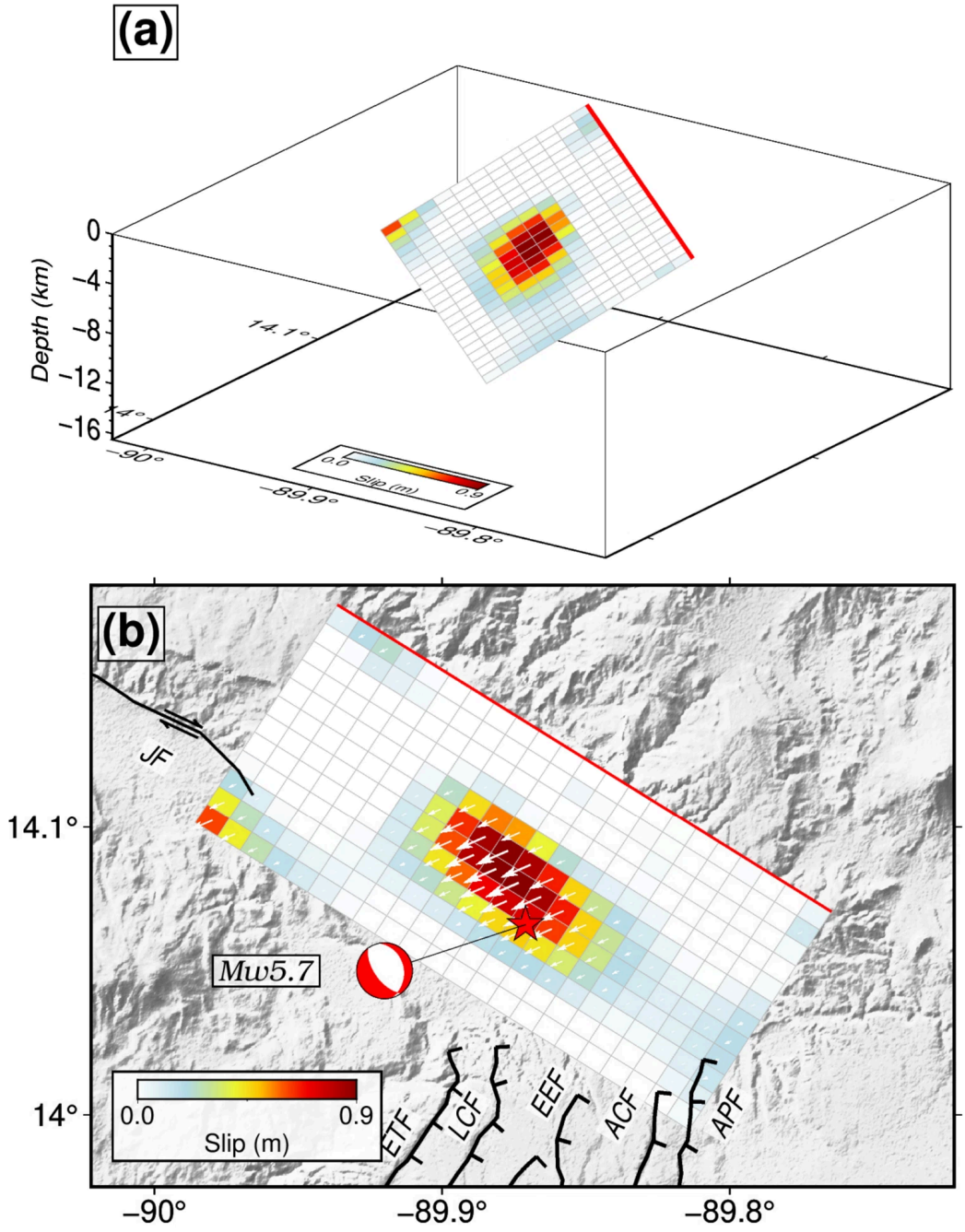


Figure 6. (**a**) is the three-dimensional view of the SW-dipping coseismic slip distribution model for the 29 July 2025 Mw 5.7 Comapa earthquake; (**b**) is the 2D map view of the slip model. Red thick line depicts the fault surface trace. The red star denotes the epicenter, and the beach ball represents the focal mechanism of this earthquake.

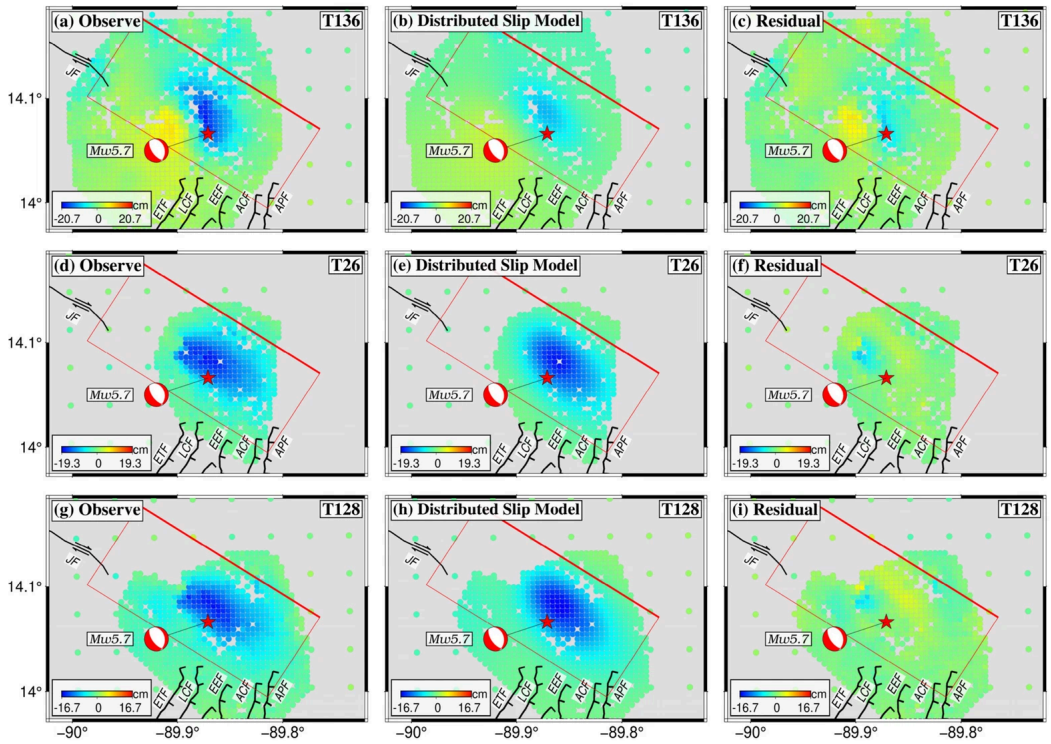


Figure 7. (**a**,**d**,**g**) are the observed coseismic surface deformation of the 29 July 2025 Comapa earthquake; (**b**,**e**,**h**) are the corresponding modeled deformation by the SW-dipping coseismic slip model of the Comapa earthquake; (**c**,**f**,**i**) are residual maps. Red box indicates the surface projection of the SW-dipping rupture fault plane for the Comapa event. Red thick line depicts fault surface trace.

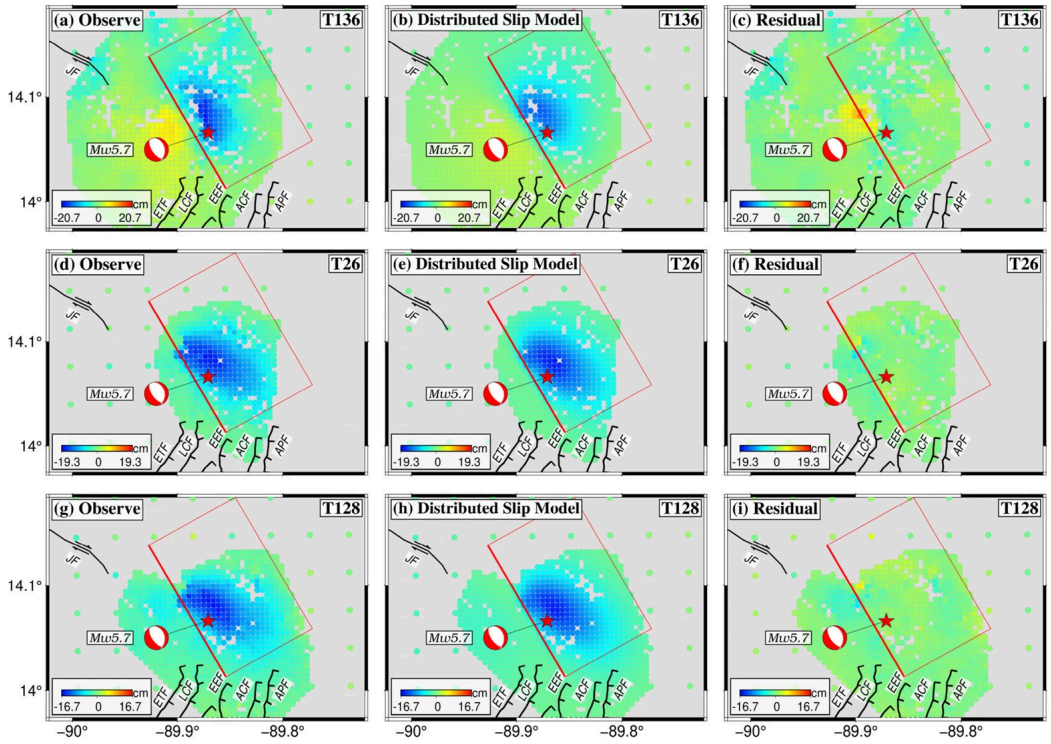


Figure 8. (**a**,**d**,**g**) are the measured coseismic surface deformation of the 29 July 2025 Comapa earthquake; (**b**,**e**,**h**) are the corresponding modeled deformation by the NE-dipping coseismic slip distribution model of the Comapa earthquake; (**c**,**f**,**i**) are residual maps. Red box indicates the surface projection of the NE-dipping rupture fault plane for the Comapa event. Red thick line depicts

fault surface trace.

4.2. Stress Interaction Between the July 2025 M_W 5.7 Comapa Earthquake and Historical Large Earthquakes

The rupture of large historical earthquakes along the major plate boundary fault systems of Central America can significantly alter the regional stress field and influence the generation of subsequent earthquakes on surrounding fault structures [19,20]. Complex tectonic loading originating from long-term plate convergence is further modulated by coseismic stress perturbations from preceding large events, which may either encourage or suppress future rupture on nearby blind and active faults. Static Coulomb stress transfer has been widely recognized as a robust mechanism for analyzing earthquake interactions, as it quantifies the change in shear stress resolved on a receiver fault plane by incorporating normal-stress effects and an effective friction coefficient. To explore whether the stress redistribution induced by historical large earthquakes promoted the rupture of the 2025 M_W 5.7 Comapa earthquake, we computed the coseismic Coulomb failure stress (CFS) changes due to the significant regional M_W > 7.0 earthquakes occurring in southern Guatemala and its adjacent regions since 1976 (Figure 1b and Table 3). These events consist of the 1976 M_W 7.5 earthquake, 1982 M_W 7.3 earthquake, 1983 M_W 7.0 earthquake, 2001 M_W 7.7 earthquake and 2012 M_W 7.4 earthquake (Figures 1b and 9 and Table 3), defining them as events A, B, C, D and E, respectively. We utilized the open PSGRN/PSCMP software [21] to perform the CFS calculation within a homogeneous elastic half-space medium. The USGS website provides the epicenter and earthquake focal mechanisms of these historical events (Table 3). The length, width and slip of the seismogenic faults for these earthquakes are calculated according to the Wells and Coppersmith empirical formula (Table 3) [22]. The earthquake focal mechanism of the 2025 M_W 5.7 Comapa earthquake (Table 1) is adopted as the receiver mechanism for stress evaluation. A typical effective friction coefficient of 0.4 is used [23]. At last, we calculate the CFS changes at 3 km depth (the depth where the maximum coseismic slip of Comapa earthquake occurs). Negative stress values generally correspond to stress unloading and inhibit rupture whereas positive values correspond to stress loading and promote it. Compared with all evaluated historical events (Figure 9), event A (the 1976 Motagua earthquake) played a key role in the long-term stress evolution of the source fault zone of the 2025 Comapa earthquake. The CFS changes induced by event A at the epicenter of the 2025 Comapa event are 0.026 MPa (Table 4). The cumulative CFS changes from all five historical events reached ~0.033 MPa at the epicentral region of the 2025 Comapa event (Table 4 and Figure 9). The stress loading exceeds the widely accepted triggering threshold of 0.01 MPa [24,25], suggesting that the surrounding historical large earthquakes may have advanced the occurrence of the 2025 M_W 5.7 Comapa earthquake.

Table 3. Source parameters of the 1976 M_W 7.5, 1982 M_W 7.3, 1983 M_W 7.0, 2001 M_W 7.7 and 2012 M_W 7.4 earthquakes acquired from the Wells and Coppersmith empirical formula [22].

Earthquake	Model	Lon, Lat (°)	Strike, Dip, Rake (°)	Depth (km)	Length (km)	Width (km)	Slp-STk (m)	Slp-Dip (m)
19 76 M $_W$ 7.5 Earthquake	USGS	−89.101, 15.324	254, 73, −10	5.0	120.23	18.4	2.65	0.47
19 82 M $_W$ 7 . 3 Earthquake	USGS	−89.387, 13.332	102, 25, −106	73.0	58.9	26.0	−0.41	1.43
19 83 M $_W$ 7.0 Earthquake	USGS	−91.924, 14.066	296, 19, 89	67.1	43.65	18.2	0	−0.66

Earthquake	Model	Lon, Lat (°)	Strike, Dip, Rake (°)	Depth (km)	Length (km)	Width (km)	Slp-STk (m)	Slp-Dip (m)
2001 M $_W$ 7.7 Earthquake	USGS	−88.660, 13.049	300, 55, −90	60.0	93.3	35.9	0	2.52
2012 M $_W$ 7.4 Earthquake	USGS	−91.895, 13.988	295, 25, 90	24.0	74.47	26.55	0	−0.71

Table 4. CFS changes caused by coseismic rupture of the 1976 M_W 7.5, 1982 M_W 7.3, 1983 M_W 7.0, 2001 M_W 7.7 and 2012 M_W 7.4 earthquakes at the epicenter of 2025 Comapa earthquake.

Coulomb Failure Stress Changes	1976 M_W 7.5 Event	1982 M_W 7.3 Event	1983 M_W 7.0 Event	2001 M_W 7.7 Event	2012 M_W 7.4 Event
CFS	0.0257 MPa	0.00294 MPa	0.0005 MPa	0.0034 MPa	0.00094 MPa

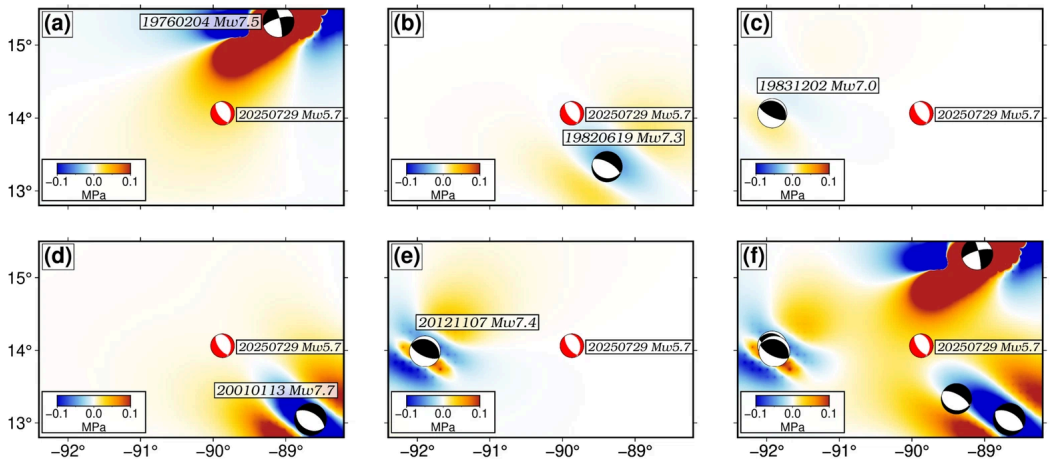


Figure 9. CFS changes at the epicentral region of the 2025 Comapa earthquake. (**a**–**e**) are coseismic CFS changes for events A–E, respectively. (**f**) is the cumulative CFS due to the five historical events. Red beach ball shows earthquake focal mechanism of the 2025 Comapa earthquake, whereas black beach balls indicate earthquake focal mechanisms of the earthquakes A–E.

4.3. Rupture Potential of Surrounding Faults

Coseismic rupture linked to the moderate-to-strong earthquakes commonly generates important changes in the regional stress field, thus altering the stress loading state of neighboring active faults. The stress redistribution may bring forward or delay subsequent earthquakes [26–29]. Such static stress perturbations do not directly trigger earthquakes instantaneously; instead, they can modify the fault stress background and alter the time-dependent seismic hazard on surrounding structures over multi-year to decadal timescales. Although static Coulomb stress modeling cannot predict the precise timing of future earthquakes, it provides qualitative constraints to identify fault segments approaching critical failure stress. To investigate the stress transfer of the 29 July 2025 Comapa earthquake sequence and its potential implications for regional seismic hazards, we quantitatively compute the static CFS changes along the neighboring active faults. The coseismic slip distribution model obtained from our geodetic modeling (Figure 5) is used as the input source model. Given that the coseismic deformation may contain contributions from the 2025 M_W 5.6 foreshock and M_W 5.7 Comapa mainshock, we attribute our inverted coseismic slip model from InSAR observations to the 2025 Comapa earthquake sequence. According to the regional fault distribution and kinemat-

ics, we adopted average strike, dip, and rake angles of 20°, 50°, and −90°, respectively, for the ETF, LCF, PPF, EEF, ACF, APF, and SVF as the receiver fault mechanisms. For the JF, the corresponding receiver fault mechanisms are set as strike, dip, and rake angles of 300°, 80°, and −180°, respectively. We performed the CFS calculations at 5 km, 10 km, and 15 km, which represent the main depth interval of brittle seismogenic faulting across the tectonic area. The stress results (Figure 10) reveal that the ETF, LCF, PPF, EEF, ACF and APF exhibit stress-unloading conditions, which may lower their short-term probability of experiencing subsequent rupture. By comparison, the shallow part of the SVF (a stress value of 0.04 MPa) and the eastern segment of the JF (a stress magnitude of 0.17 MPa) show stress loading of more than 0.01 MPa (Figure 10), implying that these fault segment accumulates greater coseismic stress perturbation from the Comapa earthquake sequence. Even though static CFS changes constitute only one component of the complete regional stress budget and long-term tectonic loading still dominates fault-scale stress evolution, such extra coseismic loading has the potential to expedite rupture on faults already close to failure. Considering the large positive coseismic stress loading on the shallow part of the SVF and the eastern segment of the JF (Figure 10), we suggest that these two fault segments deserve particular attention in future earthquake hazard evaluation.

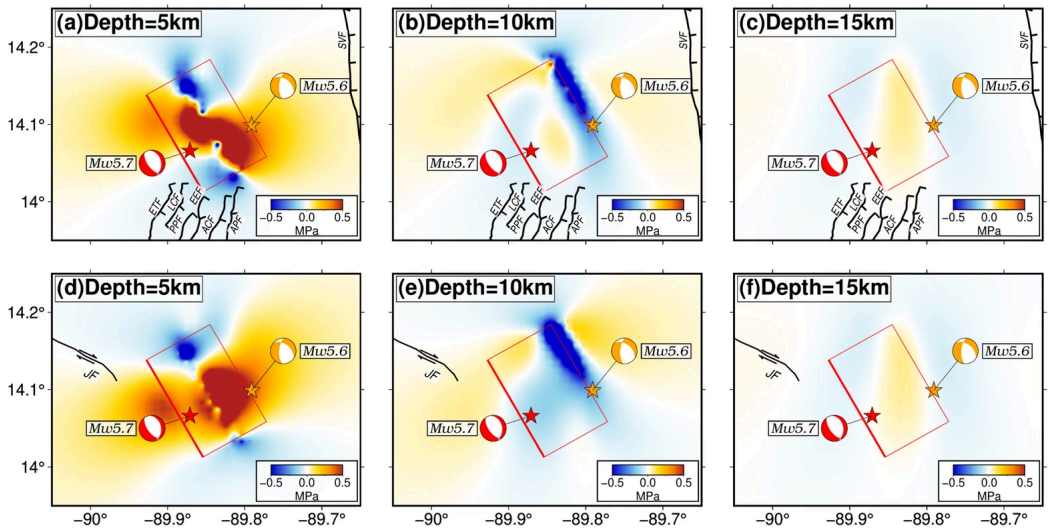


Figure 10. Coseismic CFS changes along the neighboring faults due to the 29 July 2025 Comapa earthquake sequence. (**a**–**c**) depict the coseismic CFS changes of ETF, LCF, PPF, EEF, ACF and APF at varying depths; (**d**–**f**) exhibit the coseismic CFS changes of JF at varying depths.

5. Conclusions

We use multi-orbit Sentinel-1 InSAR images to investigate the coseismic surface deformation, rupture behavior and subsurface seismogenic structure of the 29 July 2025 Comapa earthquake sequence. Based on an integrated analysis of the detailed geodetic modeling and regional tectonics and fault kinematics, we find that the Comapa earthquake sequence ruptured a previously unidentified moderate-angle NE-dipping normal fault. Most coseismic slip of up to ~0.6 m on the seismogenic fault is concentrated within depths of 0–6 km beneath the high-altitude summit. The subsidence displacement caused by the down-dip coseismic slip of this earthquake sequence lowers the local high topography and thereby shapes the regional topographic evolution. The stress interaction between the 2025 Comapa earthquake and surrounding five large historical M_W > 7.0 earthquakes is also evaluated, and the cumulative static Coulomb stress changes induced by these historical events reached ~0.033 MPa at the Comapa hypocenter, likely advancing the occurrence of this earthquake. Moreover, the significant stress loading of

0.04 MPa and 0.17 MPa along the eastern segment of the Jalpatagua fault and the shallow part of the San Vicente fault, respectively, caused by the 2025 Comapa earthquake sequence indicates that these segments warrant more attention.

Supplementary Materials: The following supporting information can be downloaded at https://www.mdpi.com/article/doi/s1. **Supplementary Text S1** : Details of InSAR processing. This text presents the InSAR data-processing procedures for source inversion, including tropospheric delay mitigation without external atmospheric correction products, removal of residual orbital errors by second-order planar ramp fitting, and sensitivity tests for the coherence-masking threshold. Corresponding validation tests demonstrate that these processing strategies introduce only limited perturbations to the inverted slip distribution.

Author Contributions: Conceptualization, J.Y. and K.M.; methodology, S.G. and J.Y.; software, J.Y. and Z.Y.; validation, K.M. and H.Z.; formal analysis, K.M. and H.Z.; investigation, S.G., H.Z. and J.Y.; resources, K.M. and Z.Y.; data curation, X.H. and J.Y.; writing-original draft preparation, J.Y., H.Z. and S.G.; writing-review and editing, J.Y., K.M., H.Z. and S.G.; visualization, K.M. and T.W.; supervision, K.M.; project administration, J.Y.; funding acquisition, J.Y. All authors have read and agreed to the published version of the manuscript.

Funding: This research is supported by the National Natural Science Foundation of China (nos. 42304007).

Data Availability Statement: The Sentinel-1 SAR images used in this study are provided by the Alaska Satellite Facility (ASF) Data Search (https://search.asf.alaska.edu/). The focal mechanism solutions for the 2025 Comapa earthquake sequence are derived from the United States Geological Survey (USGS; https://www.usgs.gov/) and the Global Centroid Moment Tensor (GCMT) project (https://www.globalcmt.org/).

Acknowledgments: The Sentinel-1A SAR data processing is performed using the SARscape® module within the ENVI software package. Most figures in this manuscript are generated using the Generic Mapping Tools (GMT 6.5) software [30].

Conflicts of Interest: The authors declare no conflicts of interest.

Abbreviations

The following abbreviations are used in this manuscript:

MAT	Middle America Trench
MPFS	Motagua-Polochic fault system
JF	Jalpatagua Fault
GG	Guatemala City graben
IG	Ipala graben
CAVA	Central American Volcanic Arc
USGS	United States Geological Survey
EMSC	Euro-Mediterranean Seismological Centre
GCMT	Global Centroid Moment Tensor
ETF	El Tigre Fault
LCF	Las Chinamas Fault
PPF	Palo Pique Fault
EEF	El Espino Fault
ACF	Ahuachapan Fault
APF	Ashapuco Fault

SVF	San Vicente Fault
ESA	European Space Agency
SAR	synthetic aperture radar
DInSAR	Differential interferometric SAR
LOS	line of sight
IW	Interferometric Wide swath
ASF	Alaska Satellite Facility

References

1. Mann, P.; Burke, K. Neotectonics of the Caribbean. *Rev. Geophys.* **1984**, *22*, 309–362. [Google Scholar] [CrossRef]
2. Guzmán-Speziale, M.; Molina, E. Seismicity and seismically active faulting of Guatemala: A review. *J. S. Am. Earth Sci.* **2022**, *115*, 103740. [Google Scholar] [CrossRef]
3. Lyon-Caen, H.; Barrier, E.; Lasserre, C.; Franco, A.; Arzu, I.; Chiquin, L.; Chiquin, M.; Duquesnoy, T.; Flores, O.; Galicia, O. Kinematics of the North American–Caribbean-Cocos plates in Central America from new GPS measurements across the Polochic-Motagua fault system. *Geophys. Res. Lett.* **2006**, *33*, 19. [Google Scholar] [CrossRef]
4. DeMets, C.; Gordon, R.G.; Argus, D.F. Geologically current plate motions. *Geophys. J. Int.* **2010**, *181*, 1–80. [Google Scholar] [CrossRef]
5. Ellis, A.; DeMets, C.; McCaffrey, R.; Briole, P.; Cosenza Muralles, B.; Flores, O.; Guzmán-Speziale, M.; Hernández, D.; Kostoglodov, V.; LaFemina, P. GPS constraints on deformation in northern Central America from 1999 to 2017, Part 2: Block rotations and fault slip rates, fault locking and distributed deformation. *Geophys. J. Int.* **2019**, *218*, 729–754. [Google Scholar] [CrossRef]
6. Franco, A.; Lasserre, C.; Lyon-Caen, H.; Kostoglodov, V.; Molina, E.; Guzman-Speziale, M.; Monterosso, D.; Robles, V.; Figueroa, C.; Amaya, W.; et al. Fault kinematics in northern Central America and coupling along the subduction interface of the Cocos Plate, from GPS data in Chiapas (Mexico), Guatemala and El Salvador. *Geophys. J. Int.* **2012**, *189*, 1223–1236. [Google Scholar] [CrossRef]
7. Styron, R.; García-Pelaez, J.; Pagani, M. CCAF-DB: The Caribbean and Central American active fault database. *Nat. Hazards Earth Syst. Sci.* **2020**, *20*, 831–857. [Google Scholar] [CrossRef]
8. Burkart, B.; Self, S. Extension and rotation of crustal blocks in northern Central America and effect on the volcanic arc. *Geology* **1985**, *13*, 22–26. [Google Scholar] [CrossRef]
9. Guzmán-Speziale, M. Active seismic deformation in the grabens of northern Central America and its relationship to the relative motion of the North America–Caribbean plate boundary. *Tectonophysics* **2001**, *337*, 39–51. [Google Scholar] [CrossRef]
10. Torres, R.; Snoeij, P.; Geudtner, D.; Bibby, D.; Davidson, M.; Attema, E.; Potin, P.; Rommen, B.; Floury, N.; Brown, M.; et al. GMES Sentinel-1 mission. *Remote Sens. Environ.* **2012**, *120*, 9–24. [Google Scholar] [CrossRef]
11. Helz, R.L. *Monitoring Ground Deformation from Space*; U.S. Geological Survey Fact Sheet 2005-3025; U.S. Department of the Interior: Reston, VA, USA, 2005.
12. Sarychikhina, O.; Glowacka, E. Spatio-temporal evolution of aseismic ground deformation in the Mexicali Valley (Baja California, Mexico) from 1993 to 2010, using differential SAR interferometry. *Proc. Int. Assoc. Hydrol. Sci.* **2015**, *372*, 335–341. [Google Scholar] [CrossRef]
13. Gabriel, A.K.; Goldstein, R.M.; Zebker, H.A. Mapping small elevation changes over large areas: Differential radar inter-ferometry. *J. Geophys. Res.* **1989**, *94*, 9183–9191. [Google Scholar] [CrossRef]
14. Goldstein, R.M.; Werner, C.L. Radar interferogram filtering for geophysical applications. *Geophys. Res. Lett.* **1998**, *25*, 4035–4038. [Google Scholar] [CrossRef]
15. Costantini, M. A Novel Phase Unwrapping Method Based on Network Programming. *IEEE Trans. Geosci. Remote Sens.* **1998**, *36*, 813–821. [Google Scholar] [CrossRef]
16. Okada, Y. Surface Deformation Due to Shear and Tensile Faults in a Half-Space. *Bull. Seismol. Soc. Am.* **1985**, *75*, 1135–1154. [Google Scholar] [CrossRef]
17. Marquardt, D.W. An Algorithm for Least-Squares Estimation of Nonlinear Parameters. *J. Soc. Ind. Appl. Math.* **1963**, *11*, 431–441. [Google Scholar] [CrossRef]
18. Wang, L.; Zhao, X.; Xu, W.; Xie, L.; Fang, N. Coseismic slip distribution inversion with unequal weighted Laplacian smoothness constraints. *Geophys. J. Int.* **2019**, *218*, 145–162. [Google Scholar] [CrossRef]

19. Lin, J.; Stein, R.S. Stress triggering in thrust and subduction earthquakes and stress interaction between the southern San Andreas and nearby thrust and strike-slip faults. *J. Geophys. Res. Solid Earth* **2004**, *109*, B02303. [Google Scholar] [CrossRef]
20. Martínez-Díaz, J.J.; Álvarez-Gómez, J.A.; Benito, B.; Hernández, D. Triggering of destructive earthquakes in El Salvador. *Geology* **2004**, *32(1)*, 65–68. [Google Scholar] [CrossRef]
21. Wang, R.; Lorenzo-Martín, F.; Roth, F. PSGRN/PSCMP—A new code for calculating co-and post-seismic deformation, geoid and gravity changes based on the viscoelastic-gravitational dislocation theory. *Comput. Geosci.* **2006**, *32*, 527–541. [Google Scholar] [CrossRef]
22. Wells, D.L.; Coppersmith, K.J. New empirical relationships among magnitude, rupture length, rupture width, rupture area, and surface displacement. *Bull. Seismol. Soc. Am.* **1994**, *84*, 974–1002. [Google Scholar] [CrossRef]
23. Freed, A.M. Earthquake triggering by static, dynamic, and postseismic stress transfer. *Annu. Rev. Earth Planet. Sci.* **2005**, *33*, 335–367. [Google Scholar] [CrossRef]
24. King, G.C.P.; Stein, R.S.; Lin, J. Static stress changes and the triggering of earthquakes. *Bull. Seismol. Soc. Am.* **1994**, *84*, 935–953. [Google Scholar] [CrossRef]
25. Harris, R.A.; Simpson, R.W.; Reasenberg, P.A. Influence of static stress changes on earthquake locations in southern California. *Nature* **1995**, *375*, 221–224. [Google Scholar] [CrossRef]
26. Liu, B.; Xie, M.; Shi, B. Effect of Qinghai Madoi MS 7.4 earthquake on Coulomb stress and earthquake probability increment of adjacent faults. *Chin. J. Geophys.* **2022**, *65*, 563–579. [Google Scholar]
27. Parsons, T.; Stein, R.S.; Simpson, R.W.; Reasenberg, P.A. Stress sensitivity of fault seismicity: A comparison between limited-offset oblique and major strike-slip faults. *J. Geophys. Res. Solid Earth* **1999**, *104*, 20183–20202. [Google Scholar] [CrossRef]
28. Symithe, S.J.; Calais, E.; Haase, J.S.; Freed, A.M.; Douilly, R. Coseismic slip distribution of the 2010 M 7.0 Haiti earthquake and resulting stress changes on regional faults. *Bull. Seismol. Soc. Am.* **2013**, *103*, 2326–2343. [Google Scholar] [CrossRef]
29. Toda, S.; Stein, R.S.; Reasenberg, P.A.; Dieterich, J.H.; Yoshida, A. Stress transferred by the 1995 M_W = 6.9 Kobe, Japan, shock: Effect on aftershocks and future earthquake probabilities. *J. Geophys. Res. Solid Earth* **1998**, *103*, 24543–24565. [Google Scholar] [CrossRef]
30. Wessel, P.; Luis, J.F.; Uieda, L.; Scharroo, R.; Wobbe, F.; Smith, W.H.F.; Tian, D. The Generic Mapping Tools Version 6. *Geochem. Geophys. Geosyst.* **2019**, *20*, 5556–5564. [Google Scholar] [CrossRef]

Disclaimer/Publisher's Note: The statements, opinions and data contained in all publications are solely those of the individual author(s) and contributor(s) and not of MDPI and/or the editor(s). MDPI and/or the editor(s) disclaim responsibility for any injury to people or property resulting from any ideas, methods, instructions or products referred to in the content.